International Journal of Applied Earth Observations and Geoinformation 114 (2022) 103023

Contents lists available at ScienceDirect

International Journal of Applied Earth Observations and Geoinformation

journal homepage: www.elsevier.com/locate/jag

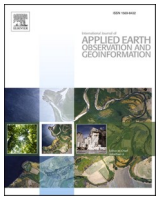

Building consistent time series night-time light data from average DMSP/OLS images for indicating human activities in a large-scale oceanic area

Rongyong Huang [a,b,1], Wenqian Wu [a,1], Kefu Yu [a,b,*]

[a] Guangxi Laboratory on the Study of Coral Reefs in South China Sea, Coral Reef Research Center of China, School of Marine Sciences, Guangxi University, Nanning 530004, China
[b] Southern Marine Science and Engineering Guangdong Laboratory (Zhuhai), Zhuhai 519000, China

ARTICLE INFO

Keywords:
Ocean
DMSP/OLS average image
Random Forest
Time series
Intercalibration

ABSTRACT

Human activities in the ocean have never been chronically and continuously investigated on a large scale. Night-time light (NTL) images collected by the Defense Meteorological Satellite Program/Operational Linescan System (DMSP/OLS) have been used as a proxy for monitoring the distribution and intensity of some human activities in the ocean from 1992 to 2013. However, systematic radiometric biases exist among the average visible-light DMSP/OLS NTL images ($DMSP_{avg}$) derived from different satellites. Moreover, the high randomness of fishing vessel locations and the large amount of noise impede the intercalibration of $DMSP_{avg}$. To address these issues, this study has developed a method for generating a series of consistent NTL images from 1992 to 2013 for a large-scale oceanic area. A composite image was first constructed by combining the original $DMSP_{avg}$, median, and standard deviation filter images derived from the $DMSP_{avg}$, and a bathymetry image. Thereafter, Random Forest (RF) algorithm was employed to classify the composite image into effective and noisy pixels. Finally, a stepwise intercalibration method was adopted to reduce the systematic radiometric biases in the denoised images. The experimental results showed that RF had an overall accuracy of 96% and a Kappa coefficient of 0.775. Furthermore, the intercalibration was shown to significantly reduce the systematic radiometric biases owing to the noises being effectively discarded by the RF. Specifically, the Sum Normalized Different Index (SNDI) of the images intercalibrated by the proposed method can reach 0.61, which is 68.2% less than that of the original $DMSP_{avg}$. In addition, the correlation coefficients between the intercalibrated $DMSP_{avg}$ and fishery catches in the exclusive economic zones (EEZs) of Japan and Malaysia can reach 0.949 and 0.901, respectively, which are higher than other values, such as the one intercalibrated using the Pseudo-Invariant Features (PIFs) method. In summary, the proposed method has been proven to be effective and feasible for generating consistent time-series NTL data for a large-scale oceanic area, and the derived Total Light Index (TLI) is an effective indicator of ocean fishery activities for ocean ecosystem research and related applications.

1. Introduction

More than 95% of the oceans are currently exposed to numerous local stressors caused by human activities (Gissi et al., 2021). The stressors include maritime vessels, overfishing activities, oil pollution from offshore wells, and construction of seaports. These stressors adversely impact marine resources (Chen et al., 2018; Jenssen 1996; Robards et al., 2016). For example, overfishing is considered the main reason for the reduction in global fishery resources and it is agreed that production has reached its limits (Derrick et al., 2017). Moreover, fishery resources have declined dramatically in some regions (Rodhouse et al., 2001). Therefore, for sustainable development and conservation of marine resources, it is crucial to monitor human activities in marine areas.

Some mandatory vessel communication and navigational safety systems, such as the Automatic Identification System (AIS) and Vessel Monitoring Systems (VMS), have been adopted to monitor maritime vessels to enable research on the conservation of marine resources (Robards et al., 2016). However, these systems are not satisfactory for monitoring human activities in large areas of the oceans, because the

* Corresponding author at: Guangxi Laboratory on the Study of Coral Reefs in South China Sea, Coral Reef Research Center of China, School of Marine Sciences, Guangxi University, Nanning 530004, China.
E-mail addresses: kefuyu@scsio.ac.cn, kefuyu@gxu.edu.cn (K. Yu).
[1] These authors contributed equally to this study.

https://doi.org/10.1016/j.jag.2022.103023
Received 7 August 2022; Received in revised form 8 September 2022; Accepted 13 September 2022
Available online 22 September 2022

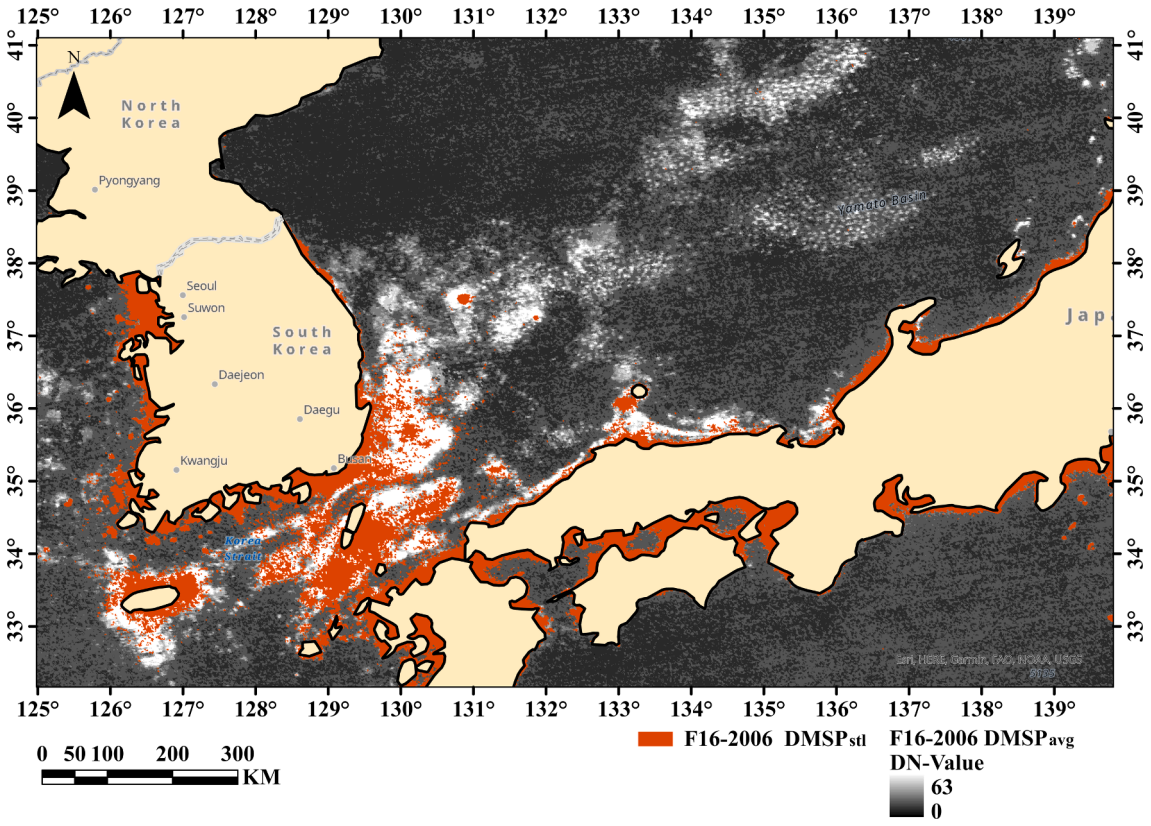

Fig. 1. Schematic diagram of the illuminated pixel comparison between the $DMSP_{avg}$ and $DMSP_{stl}$. $DMSP_{stl}$: DMSP/OLS stable light image; $DMSP_{avg}$: DMSP/OLS average visible light image.

heterogeneous data from these systems are neither publicly available nor do they cover the global scope (Kroodsma et al., 2018). Moreover, these systems can artificially turn off or tend to produce fake positioning information to avoid administration management. Therefore, the data recorded by these systems may not be comprehensive. Moreover, some countries do not use monitoring systems; for example, the Philippines did not require domestic fishing vessels to use the VMS system before 2018.

In contrast to the data recorded by electronic vessel monitoring systems, Night-time light (NTL) remote sensing images can provide a synoptic view of human activity for monitoring in both regulated and unregulated areas, that is, satellite imagery is not restricted by political boundaries. Two types of major NTL images are used for human activity research. One type is provided by the Defense Meteorological Satellite Program (DMSP)/Operational Linescan System (OLS). The DMSP/OLS satellite was designed to capture faint moonlight reflected from clouds at night for meteorological applications. Meanwhile, scientists have discovered that DMSP/OLS can also record the light emitted by urban human activities covering large areas at a low cost (Elvidge et al., 1997; Li et al., 2016; Li et al., 2017a; Shi et al., 2016). The other type is provided by the Suomi National Polar Partnership (SNPP) satellite-Visible Infrared Imaging Radiometer Suite (VIIRS). When compared with the DMSP/OLS images, SNPP-VIIRS images are calibrated in-flight with a higher spatial resolution and lower detection limits (Elvidge et al., 2013). The superior SNPP-VIIRS NTL images were effective in detecting fishing vessels and constructing time-series assessments (Elvidge et al., 2018; Elvidge et al., 2015; Ruiz et al., 2020), but most studies based on SNPP-VIIRS covered only a small or middle ocean area. However, as the SNPP satellite was launched in 2011, earlier research data is not available. For this reason, DMSP/OLS NTL images, which span a long time from 1992 to 2013, are crucial for ocean human activity research. For example, studies on live coral cover from 2004 to 2015 around Weizhou Island and the corresponding remote-sensed environmental parameters, Huang et al., (2019) concluded that eutrophication of seawater induced by human-activity may be the main cause of the degradation of live coral cover around Weizhou Island.

Except for the DMSP/OLS-NTL-image-based research on the national socioeconomic and urbanization (Cheng et al., 2016; Jin et al., 2017; Shi et al., 2016; Shi et al., 2017), DMSP/OLS NTL images can also be used to indicate human activities associated with oceanic areas, such as fishing vessels, offshore wells, and seaports (Aubrecht et al., 2008; Lu et al., 2020; Waluda et al., 2004). As early as 1978, some scholars studied the production activities of Japanese fishing boats catching squid based on single-pass DMSP/OLS NTL images (Croft 1978). Maxwell et al. (2004) conducted aerial surveys to obtain the number of squid fishing vessels on the water surface. Thereafter, a regression model was established between the number of vessels and the number of detected light pixels. Waluda et al. (2004) constructed a regression model for illuminated pixels in DMSP/OLS images and they elucidated the number of vessels derived from ARGOS data in Peruvian waters. The results showed that the estimated number of fishing vessels was correct at 83% within $\pm$ 2 vessels for 130 single-pass DMSP images from 1999. Moreover, DMSP/OLS images can also be used to survey offshore petroleum facilities (Elvidge et al., 2009). In summary, DMSP NTL images have great potential for use in studying the impacts of human activities on marine ecosystems.

However, at present, the widely used single-pass DMSP/OLS NTL images used in previous research for monitoring fishing vessels on the ocean surface are not publicly available (Cheng et al., 2017; Kiyofuji and Saitoh 2004; Waluda et al., 2008; Waluda et al., 2011; Waluda et al., 2004). Instead, annual DMSP/OLS version-4 time-series products were published to replace early products (Cheng et al., 2017). More seriously, inconsistencies caused by systematic radiometric biases existed in the annual time-series images, as there were subtle differences in performance among the multiple satellites. Moreover, on-board calibration and gain parameters of DMSP/OLS satellites are lacking (Pandey et al.,

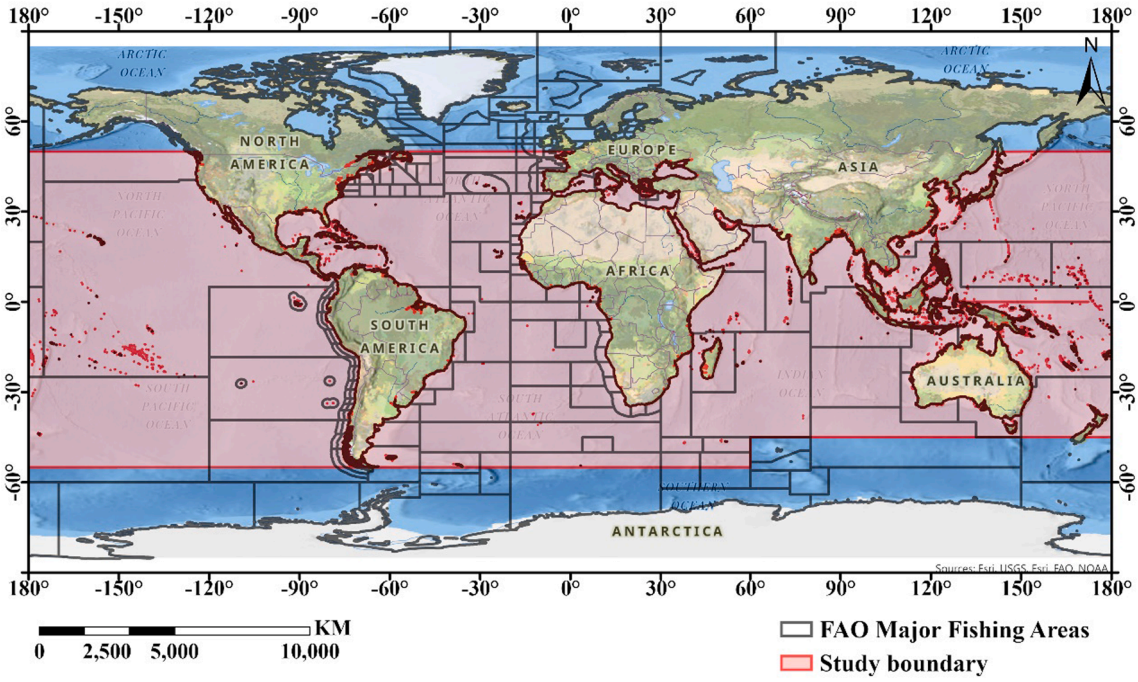

Fig. 2. Overview of study area: the study area is marked using the red rectangle, and the boundary of FAO MFAs is marked using the medium-grey lines. (For interpretation of the references to colour in this figure legend, the reader is referred to the web version of this article.)

2017). As a result, few studies have focused on the impacts of direct human activities, such as the effect of fishing vessels, on changes in marine ecosystems. For example, some researchers have analyzed the influence of other factors on the degradation of coral reefs, such as global warming (Liu et al., 2020a; Liu et al., 2020b), atmospheric nitrogen deposition (Chen et al., 2019), and human-activity-induced water eutrophication (D'Angelo and Wiedenmann 2014; Li et al., 2017b); however, detailed discussions of the impact of direct human activities on coral reef degradation have rarely been reported. In other words, DMSP/OLS NTL images cannot be utilized to quantitatively monitor changes in human activities unless they are calibrated (Pandey et al., 2017).

Intercalibration has generally been employed to reduce inconsistency. The Pseudo-Invariant Features (PIFs) method has been widely applied to the intercalibration of DMSP/OLS annual time series images for urban study (Elvidge et al., 2011; Zhang et al., 2016). The PIFs paradigm assumes that the NTL intensity is stable, and the NTL changes are only induced by systematic biases in the pseudo-invariant region. Thus, all the images pending calibrating can then be calibrated to the reference image using an empirical model, where the parameters of the model are commonly estimated using the pseudo-invariant regions. For example, Wu et al. (2013) in their study selected Mauritius, Puerto Rico, and Okinawa as pseudo-invariant regions, and intercalibration was performed using a power function model. However, because of the high randomness of fishing vessels in terms of number and location, it is unreasonable to assume a stable region in the ocean area.

The Version-4 DMSP/OLS product collection includes three subtypes of images: cloud-free, average visible light ($DMSP_{avg}$), and stable light images ($DMSP_{stl}$). $DMSP_{stl}$ which excludes sunlit, moonlit, cloudy impact, and major noise pixels, has been widely used in urban areas (Li and Zhou 2017; Liu et al., 2016; Liu et al., 2012; Pandey et al., 2017; Zhang et al., 2016). However, many of the illuminated pixels caused by human activities in the ocean were also excluded from $DMSP_{stl}$, as shown in Fig. 1. Therefore, in this study, $DMSP_{avg}$ was selected to generate consistent NTL images. Because post-compositing filtering has not been performed, a large amount of noise exists in the $DMSP_{avg}$. However, the DN values of the non-noise pixels on the ocean are small and very close to those of the noise pixels, where the DN values of the noise pixels generally fluctuated in the range of 1 to 7.

Consequently, the objectives of this study are to reduce the inconsistency caused by the systematic radiometric biases and then build consistent time series NTL images from $DMSP_{avg}$ for large-scale ocean areas during the period 1992–2013. The main idea is to combine a Random Forest (RF) algorithm with a stepwise intercalibration approach. The advantage is that the noise of the $DMSP_{avg}$ and the impacts of the highly random fishing vessel number and locations can be efficiently weakened during intercalibration. In addition, the discussion on the correlation between TLIs and fishery catches not only provides a supplement to confirm the effectiveness of the proposed method, but it also implies that the TLIs can be used as an effective indicator of fishery activities for ocean ecosystem research and for various applications in the future.

2. Material and methods

2.1. Study area and datasets

$DMSP_{avg}$ was downloaded from the National Oceanic and Atmospheric Administration (NOAA) National Geophysical Data Center (NGDC) (https://www.ngdc.noaa.gov/eog/download.html). It has a radiometric resolution of 6 bits, that is, the DN values range from 0 (no lighting) to 63 (highest lighting). The spatial resolution is 30 arc seconds (about 1-km spatial resolution at the equator). As shown in Table A1, the data was acquired by using six different satellites spanned from 1992 to 2013: F10, F12, F14, F15, F16, and F18. The quality of $DMSP_{avg}$ decreases as latitude increases (Wu et al., 2013). To avoid the impacts of high latitude area distortion and abnormally high DN-value pixels, the research boundary was established by using the data from the Food and Agriculture Organization of the United Nations (FAO) Major Fishing Areas (MFAs). Specifically, the research area covered the area between −180° to 180° longitude and −55° to 50° latitude, as shown in Fig. 2. Pixels in inland and pole regions were excluded. The FAO MFAs dataset was downloaded from GeoInfo (https://www.fao.org/fishery/area/search/en). The dataset used was determined in consultation with

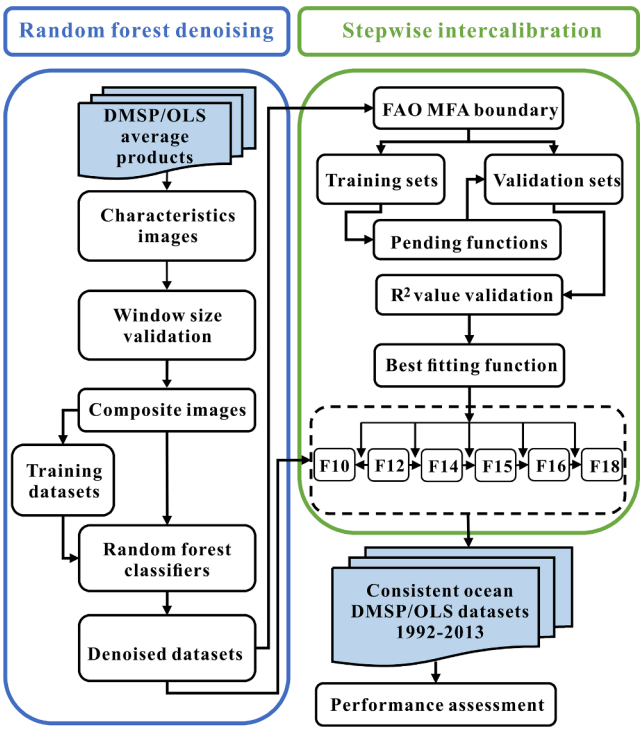

Fig. 3. Framework of the proposed method.

international fishery agencies on various considerations, such as the boundary of natural regions and the natural divisions of the seas.

Exclusive Economic Zones (EEZs) were selected to conduct the assessments. These EEZs include China (CHN), Indonesia (IDN), Japan (JPN), Malaysia (MYS), Thailand (THA), Vietnam (VNM), Peru (PUR), United States (USA), and Argentina (ARG). The boundaries of the EEZs were provided by the Maritime Boundaries Geodatabase, downloaded from the Marineregions website (https://www.marineregions.org/sources.php#marbound).

As bathymetry was considered a factor for the formation of a marine fishing area (Ruiz et al., 2020), bathymetric data were also considered as a feature to identify the noise. Bathymetry data were provided by the General Bathymetric Chart of the Oceans (GEBCO). The GEBCO_2014 version data with a 30'' spatial resolution was used (https://www.gebco.net/data_and_products/historical_data_sets/#gebco_2014).

Fishery catch data (1950–2016) were used as auxiliary data to highlight the significance of this study in regards to fishery management and assessment. The data can be downloaded from the research initiative, Sea Around Us (https://www.seaaroundus.org/simple-site.php#/eez). The data are regarded as an accurate measure for marine fisheries at the country level (Golden et al., 2016).

The intercalibration coefficients derived from the PIFs method proposed by Elvidge et al. (2014) were also used to intercalibrate the denoised images. The purpose was to compare the proposed method with the PIFs method.

2.2. Methods

The proposed method consisted of two parts. First, Random Forest (RF) algorithm was applied to identify the effective pixels. Second, the inconsistency of the denoised images is reduced using a stepwise intercalibration approach. Here, effective pixels are defined as pixels in the $DMSP_{avg}$ that can record the light emitted by marine human activities. The main source of light is fishing activity. The light emitted from offshore oil, gas wells, and coastal cities was also included. Fig. 3 illustrates the details of the proposed methodology.

2.2.1. Random forest denoising

As the radiance of the light emitted from fishing vessels is weaker than that of city lights, the DN values of the effective pixels in marine areas are usually lower than those in city areas. The DN values of the

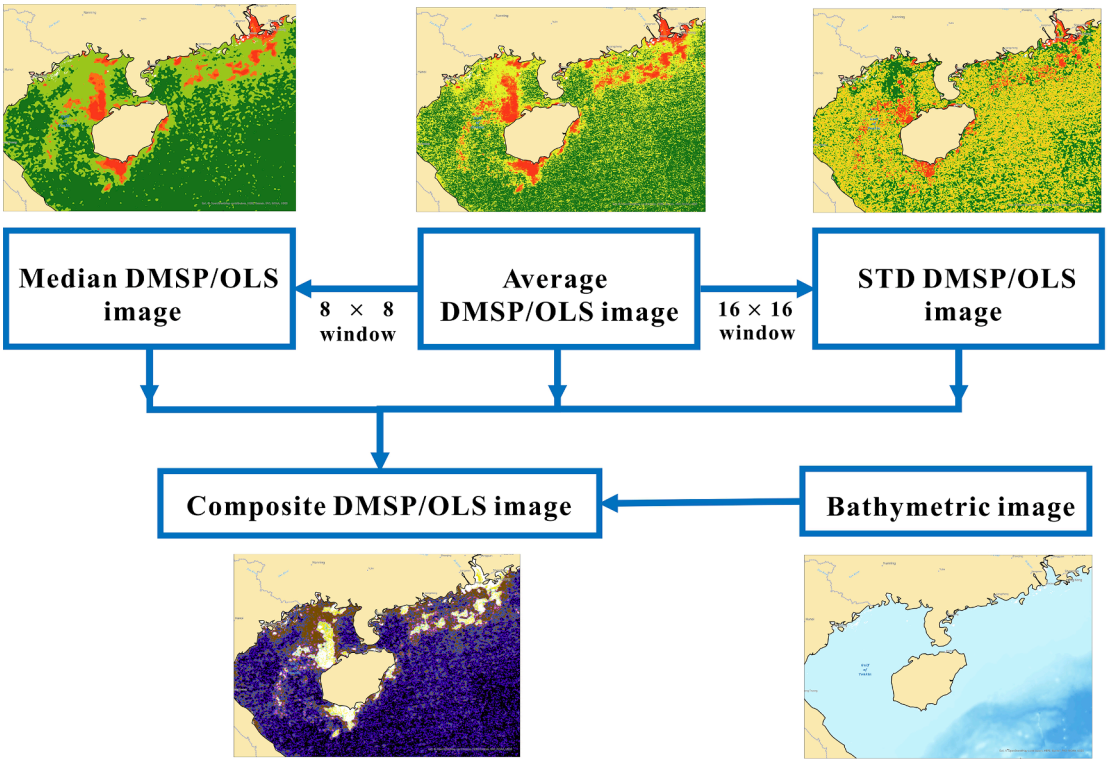

Fig. 4. Construction of a composite image for distinguishing the effective and the noisy pixels.

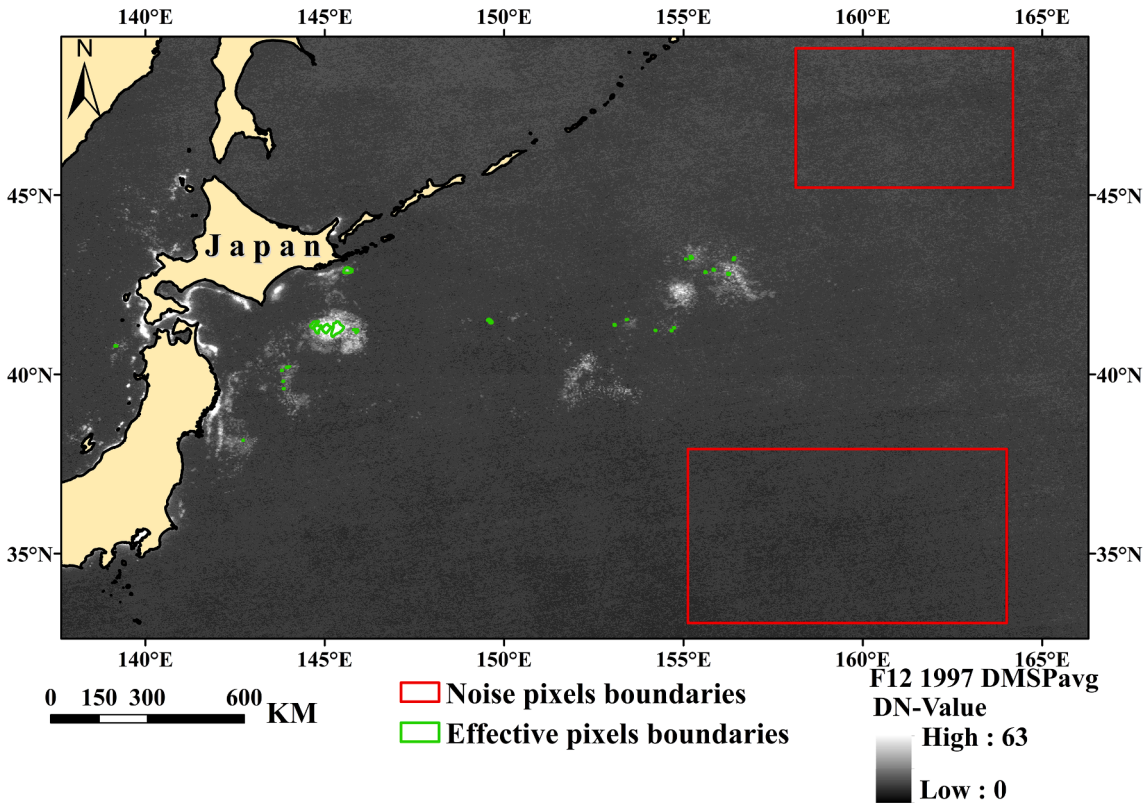

Fig. 5. Example of the selection of the training and validation pixels for constructing the RF.

Table 1
List of the reference and intercalibrated images for each step in the approach used in this study.

Step	Reference images	Intercalibrated images
1	F12-1994	F10-1992 ~ 1994
2	F12-1997 ~ 1999	F14-1997 ~ 2003
3	F14-2003	F15-2003 ~ 2007
4	F15-2004 ~ 2007	F16-2004 ~ 2009
5	F18-2011	F18-2010
6	F16-2009	F18-2010 ~ 2013

effective pixels are typically close to those of the noise pixels. What is worse, as there are nearly no human activities in many ocean areas far from inland, most of the pixels in such areas are noisy.

For studies on the NTL in urban areas, the saturation and diffusion effects in DMSP/OLS images are usually considered as data defects, which limit the application potential of the NTL data (Zhao et al., 2019a). However, for oceanic areas, as most of the light is emitted by fishing boats, such relatively low radiance makes most of the pixels unsaturated. Conversely, as diffusion effects, an NTL image is usually shown as clustered round spots with high DN values of central pixels and low DN values of surrounding pixels (Zhao et al., 2019a).

Meanwhile, it is important to consider that there is no diffusion effect for the noise pixels, that is, the noise usually presents the characteristics of a large-scale and discrete distribution. In addition, the DN values of the noise pixels increased slightly across the high-cloud coverage and high-latitude sea areas.

When considering such differences between the light emitted by human activities in the ocean and noise, a Median Filter Image (MFI) and a Standard Deviation Image (STDI) were utilized to extract the light targets. In other words, to make full use of the differences, a median filter was used to filter the noise, and a variance filter was used to enhance the edge of the light target.

In addition, as bathymetry was considered a factor for the formation of a marine fishing area (Ruiz et al., 2020), bathymetric data were also adopted as a feature to distinguish between effective pixels and noise.

In summary, $DMSP_{avg}$ was combined with the corresponding MFI, STDI, and the bathymetry to make a composite image, as shown in Fig. 4.

Thereafter, the Random Forest (RF) algorithm proposed by Breiman (2001) was applied to the composite image to identify the effective pixels and noise. The RF algorithm uses bootstrap aggregation to integrate multiple decision trees, and the classification derives from the majority vote of all individual trees (Hu et al., 2022). The reasons why RF was used are as follows: 1) RF does not require an implicit assumption on data distribution, and it is capable of accommodating different types and scales of input data (Puttanapong et al., 2022); 2) Feature importance can be easily estimated by using Mean Decrease Accuracy (MDA) or Mean Decrease Gini (MDG) (Hu et al., 2022), which helps to illustrate the necessity of each of the features for the classification; 3) RF has been applied to geospatial data and yielded a high prediction performance (Hu et al., 2022; Jin et al., 2014; Kedia et al., 2021; Puttanapong et al., 2022; Tian et al., 2022; Zhao et al., 2019b).

Furthermore, the RF is easy to handle as the major hyperparameters can conveniently be set as follows (Hu et al., 2022; Stefanski et al., 2013): 1) the number of features was set to 2, that is, the square root of the feature number in the composite image; 2) the number of trees was set to 10, where the out-of-bag (OOB) error rate began to become almost stable and was approximate to the minimum (Fig. A1). As shown in Fig. A1, the OOB error curve do not exist an apparent minimum as it was seen to be monotonically decreasing with the increase of the number of trees. For this reason, such tree number selection can limit the number of trees to being too large. This is able to reduce the probability of the RF overfitting.

The training and validation pixels of the RF were manually selected using visual interpretation, as illustrated in Fig. 5. The rules are as follows: 1) the noise pixels were mostly selected from the areas that are far

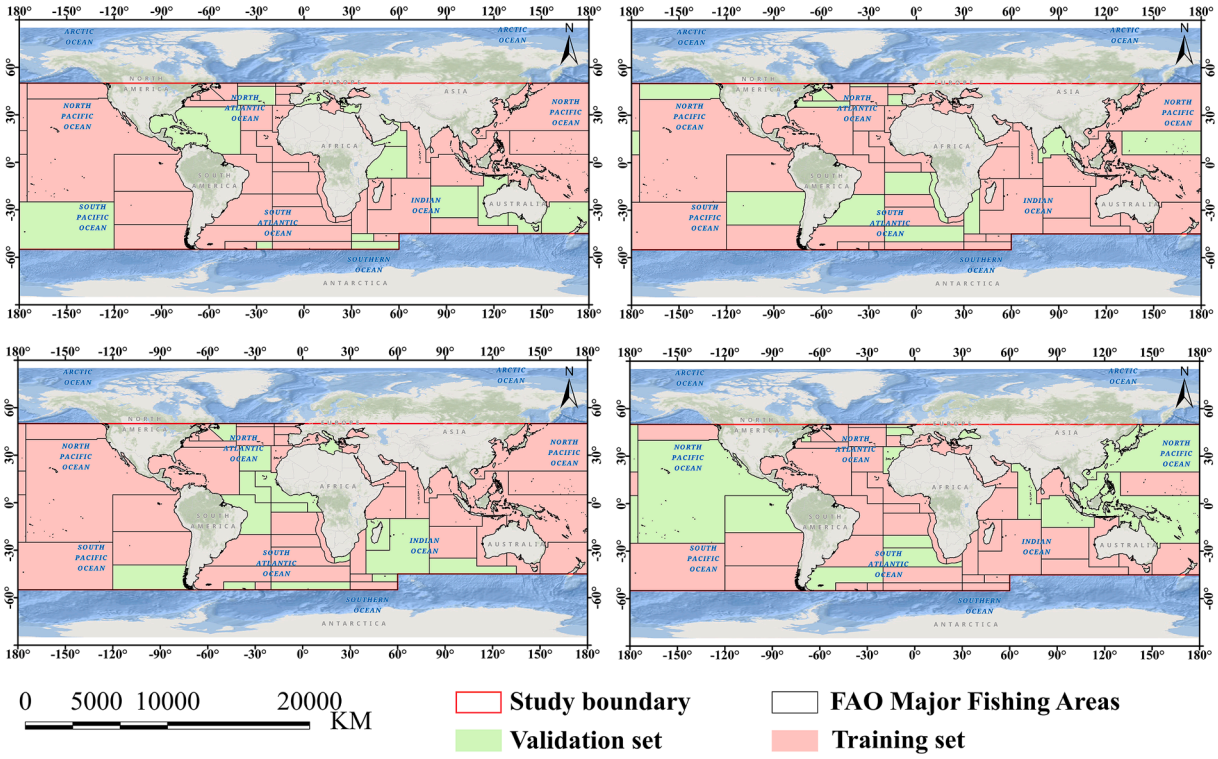

Fig. 6. Four different groups of training and validation sets derived from the FAO MFAs.

away from traditional fishing operation and coastal zones; 2) some pixels in high-latitude ocean areas were also selected as noise pixels; 3) some of the prominent bright pixels in the nearshore and traditional fishery areas were selected as the effective pixels; 4) the training pixels and the validation pixels were selected as evenly as possible.

To dissolve the overfitting problem, the training set and the testing set were selected separately and were ensured to be nonoverlapping. Specifically, the proportion between the size of the training data and that of the testing one was controlled to around 8:2 as possible, and the numbers of the training and testing pixels were controlled to no less than 300, 000 and 75, 000 pixels respectively.[2] Furthermore, during the training approach, about 37% of training data was not picked during the sampling procedure and thus was not used to train the model. Such data are known as OOB data, and error rates estimated by using the OOB data are called OOB error rates (Hu et al., 2022; Stefanski et al., 2013). As described previously, OOB error rates were utilized to determine tree number of the RF, where the probability of overfitting was reduced by limiting the number of trees to being too large.

To determine the window sizes for the calculations of MFIs and STDIs, F10-1992, F12-1996, F14-2001, F15-2002, F16-2005, and F18-2010 were used as sample images. Thereafter, different window sizes were traversed to calculate the MFIs and STDIs to construct the different composite images. RF was then applied to these composite images to classify the noise and effective pixels. Consequently, the averages of the Kappa values for the sample images were estimated. The window size corresponding to the maximum of the average Kappa values was then selected to calculate the MFIs and STDIs for all images.

2.2.2. *Stepwise intercalibration*

Owing to the high randomness of the fishing vessel locations, it was difficult to apply the PIFs method to conduct the intercalibration. However, there were several fishing boat positions that remain unchanged for a short period when they were fishing and emitting light. For example, Guo et al., (2017) proved that most of the fishing boat positions in the SNPP-VIIRS NTL image can match the VMS data within 4 h. To sufficiently utilize this situation, a stepwise intercalibration approach, referring to Li and Zhou (2017), was applied to reduce the radiometric biases of the denoised images. In the approach of Li and Zhou (2017), F12 images were utilized as reference images because the pattern of TLI derived from F12 had a stable upward trajectory. Similarly, F12 images were also selected as reference images in this study, as shown in Table. 1, the intercalibration steps are different though, as follows:

1) Instead of non-intercalibration between F10 and F12, F10 (1992–1994) was calibrated using F12-1994 as the reference image. This was because the inconsistencies between F10 and F12 were much more serious in nature in the ocean area than in the inland area.
2) Instead of combining PIFs with stepwise intercalibration, F16 (2004–2009) was intercalibrated directly by referencing the intercalibrated F15 (2004–2007). One reason is that the inconsistencies between F15-2007 and F16-2007 in the ocean area were much smaller than those in inland areas. Another reason is that the PIFs method is unreasonable in ocean areas.
3) F18-2010 was calibrated by referencing F18-2011 before F18 (2010–2013) was calibrated by referencing F16-2009. This is because F18-2010 had an extremely high TLI, whereas F18-2011 had a more reasonable trajectory.

Many functions, such as linear, quadratic, cubic, power, and exponential, have been applied to establish an intercalibration model between the pending and reference images (Li et al., 2017a; Li and Zhou 2017; Pandey et al., 2017; Wu et al., 2013; Zhao et al., 2019a). In this study, linear, quadratic, cubic, power, and exponential functions were selected as candidate pending functions.

[2] As the training set and the testing set were selected separately, the proportion between the size of training data and that of testing one is difficult to exactly control to 8:2.

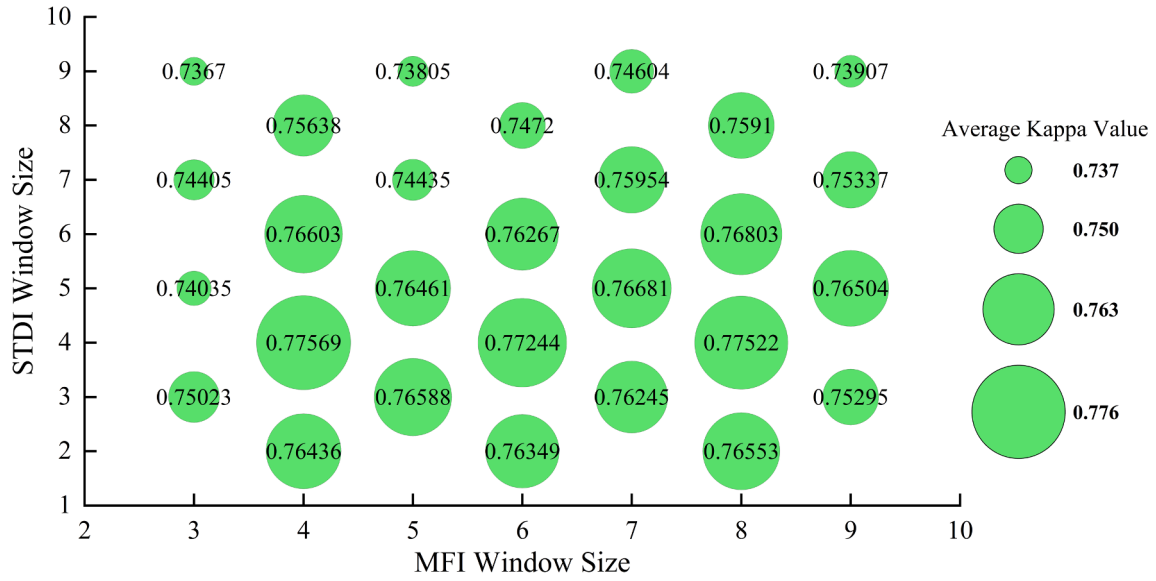

Fig. 7. Average Kappa values of the RF denoises for F10-1992, F12-1996, F14-2001, F15-2002, F16-2005, and F18-2010 images corresponding to the different window sizes for the MFI and the STDI calculations.

$$DN_c = a \times DN_p + b \tag{1}$$

$$DN_c = c \times DN_p^2 + d \times DN_p + f \tag{2}$$

$$DN_c = g \times DN_p^3 + h \times DN_p^2 + i \times DN_p + j \tag{3}$$

$$DN_c = k \times DN_p^l + m \tag{4}$$

$$DN_c = n \times e^{q \times DN_p} \tag{5}$$

where DN_p is the DN value of the pending image; DN_c is the corresponding DN value of the intercalibrated image; a, b, c, d, f, g, h, i, j, k, l, m, n, and q are the unknown coefficients of the functions.

To select the best-fitting function from all the candidate pending functions, the study area was divided into several sub-regions using FAO MFAs, as shown in Fig. 6. Some of the subregions were randomly selected as the validation set, and the rest were selected as the training set. The four different groups of the training and validation sets are shown in Fig. 6. Eqs. (1) – (5) were then trained and validated using each group of training and validation sets, respectively. Similar to Wu et al. (2013), for each step of the intercalibration, the function with the highest average coefficient of determination (R^2) and the smallest average Root Mean Square Error (RMSE) for the four validations was chosen as the best fitting function. The best-fitting functions were then applied for intercalibration.

2.2.3. Performance assessment

The Total Light Index (TLI) is widely used to indicate the intensity of human activities at the global, national, or regional levels (Elvidge et al., 2011). The intercalibration of the NTL images can be evaluated by comparing the TLI before and after intercalibration (Pandey et al., 2017). The Normalized Difference Index (NDI) was used to evaluate the inconsistencies (Zheng et al., 2019). Accordingly, the summed-up NDI (SNDI) was used to indicate the performance of the intercalibration. Here, the TLI, NDI, and SNDI were calculated using Eqs. (6) – (10) as follows:

$$TLI_{i,j} = \sum_{k=1}^{n} DN_{i,j,k} \tag{6}$$

where i, j, and k represent the satellite, year, and pixel of the NTL image, respectively; and n represents the number of pixels.

$$NDI_j \underline{\underline{\text{def}}} NDI_{r,s,j} = \frac{|TLI_{r,j} - TLI_{s,j}|}{TLI_{r,j} + TLI_{s,j}} \tag{7}$$

where r and s represent two different satellites and j represents the year of the NTL image.[3]

$$SNDI = \sum_{j}^{T} NDI_j \tag{8}$$

$$j \in T = (1994, 1997, 1998, 1999, 2003, 2004, 2005, 2006, 2007, 2009)$$

Considering that some lit pixels can be found in $DMSP_{stl}$, SNDI of these lit pixels (*pixel_SNDI*) was utilized as an auxiliary index to assess inconsistencies. The *pixel_SNDI* was calculated as follows:

$$pixel\_NDI_j \underline{\underline{def}} pixesl\_NDI_{p,s1,s2,j} = \sum_{p}^{S} \frac{|DN_{p,s1,j} - DN_{p,s2,j}|}{DN_{p,s1,j} + DN_{p,s2,j}} \tag{9}$$

$$pixel\_SNDI = \sum_{j}^{T} pixel\_NDI_j \tag{10}$$

where $p \in S$, $\boldsymbol{S}$ is the position set of the lit pixels, s_1 and s_2 represent two different satellites, j indicates the year.

Finally, as DMSP/OLS NTL single-pass images have been shown to correlate with the fishery catch in some ocean areas (Saitoh et al., 2010; Waluda et al., 2008), correlations between the TLIs and fishery catches for the EEZs of Japan and Malaysia were also conducted to verify the effectiveness of the proposed method. There were few offshore gas flaring in these EEZs (Lu et al., 2020).

3. Results

3.1. Results of the RF denoising

1) Selection of the window sizes for the MFI and the STDI calculations

[3] As there are no overlap images captured from two different satellites during 2009, NDI_{2009} was just calculated by using $TLI_{F16,\ 2009}$ and $TLI_{F18,2010}$ in this paper.

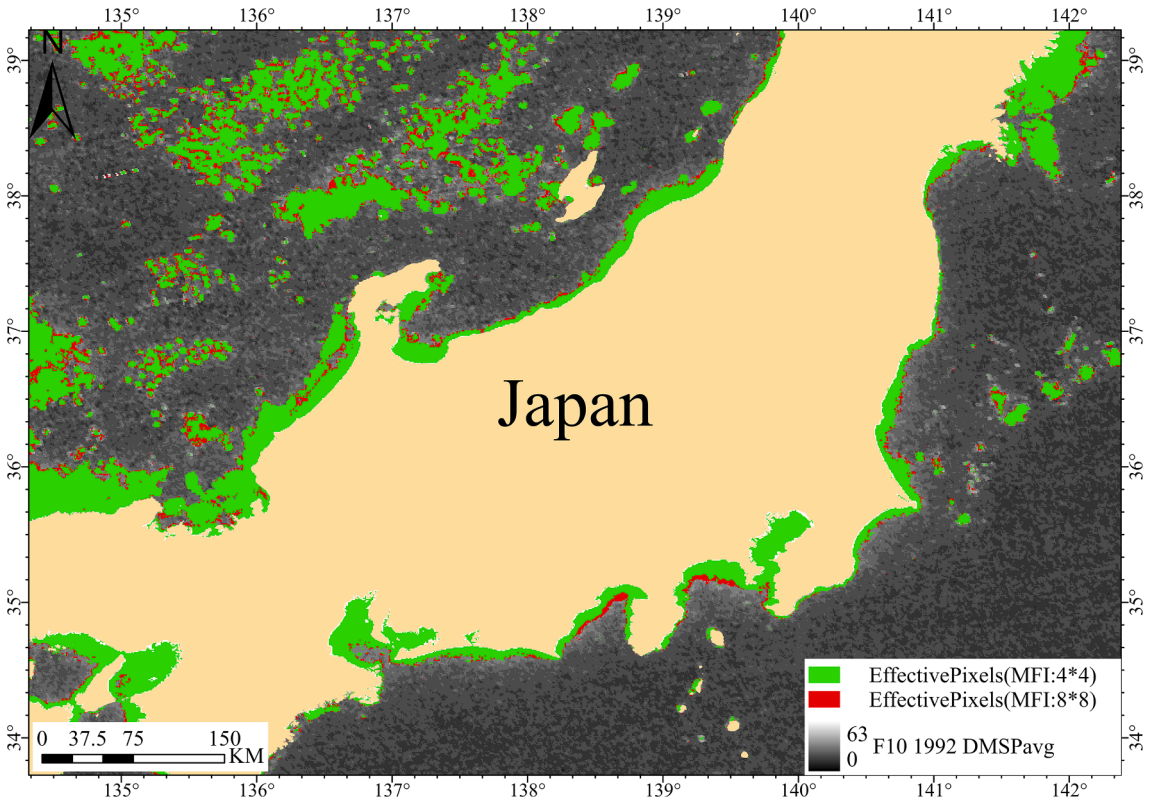

Fig. 8. Effective pixels identified by the RFs based on 4 × 4 window size and 8 × 8 window size, respectively, for the MFI calculations.

The average Kappa values of the RF denoising approaches using different window sizes corresponding to the MFI and STDI calculations are shown in Fig. 7. As shown in Fig. 7, the highest Kappa value of 0.775 was obtained when the window sizes of the MFI and STDI calculations were both 4× 4. However, the average Kappa values are very close to each other when the window size of the MFI calculation varies from 4 × 4 to 8 × 8 but the window size of the STDI calculation is fixed at 4× 4. Further comparisons showed that if the window size of the MFI calculation was chosen to be 8× 8, the identified effective pixels would become larger than those of the 4× 4 or 6× 6 window sizes. As shown in Fig. 8, most of the increased pixels are located at the edges of the diffusion effect pixels. We believe that it is reasonable that such pixels are regarded as effective pixels, so a window size of 8× 8 was finally chosen to calculate the MFIs.

2) Importance of each component of the composite image input for RF denoising

The importance scores of $DMSP_{avg}$, MFI, STDI, and bathymetry of each composite image during RF are shown in Fig. 9, where the importance scores were estimated by using MDG. The average importance scores of $DMSP_{avg}$, MFI, STDI, and bathymetry were 43%, 34%, 16%, and 7%, respectively. Overall, $DMSP_{avg}$ was the most important feature, whereas bathymetry was the most unimportant feature.

However, this does not mean that bathymetry needs to be discarded from the composite image input for the RF denoising approach. This is because the importance score of the bathymetry was higher than the STDI or MFI over several years, as shown in Fig. 9. In other words, $DMSP_{avg}$, MFI, STDI, and bathymetry are all necessary for RF denoising.

3) Accuracy of the RF denoise approach

The RF denoising approach was compared with a fixed Threshold (TS) denoising method, where a DN value of 6 was selected as the fixed TS, this effectively means that if the DN value of a pixel is not greater than 6, then the pixel is removed as noise; otherwise, the pixel is retained as an effective pixel.

This TS method was utilized for the comparison because of the following points:

1) The TS method is typically used to remove noise in urban NTL images (Zhao et al., 2019a), and 6 is typically chosen as the TS (Elvidge et al., 2011; Liang et al., 2019).
2) Histogram analyses of $DMSP_{avg}$ in the mid-high latitude ocean area indicated that more than 99.9% of the pixels had a DN value lower than 6. Thus, the maximum DN value of the major abnormal pixels in the mid-high-latitude ocean areas is generally regarded as 6.

The average overall accuracy and Kappa value of the TS method were 94.3% and 0.558, respectively. They were lower than those of the RF approach, that is, the average overall accuracy and average Kappa value of the RF approach were 96.0% and 0.775, respectively. Furthermore, the producer accuracy of the effective pixels was 45.0% for the TS method, which is significantly lower than that of the RF approach (77.8%). In other words, in contrast to the RF approach, the TS method misclassifies too many effective pixels as noise.

3.2. Results of the fitting functions of the intercalibration

Fig. 10 illustrates the average R^2 and RMSEs for each step in Table. 1. According to Eqs. (1)–(5), each step of the intercalibration includes five groups of average R^2 and the average RMSEs. As seen in the figure, the power function has the highest average R^2 and the smallest average RMSE for steps 1 and 6, whereas the cubic function has the highest average R^2 and the smallest average RMSE for steps 2, 3, 4, and 5. Therefore, the power function (Eq. (4)) was selected as the best-fitting function for steps 1 and 6, and the cubic function (Eq. (3)) was applied in steps 2, 3, 4, and 5. The coefficients of the best-fitting

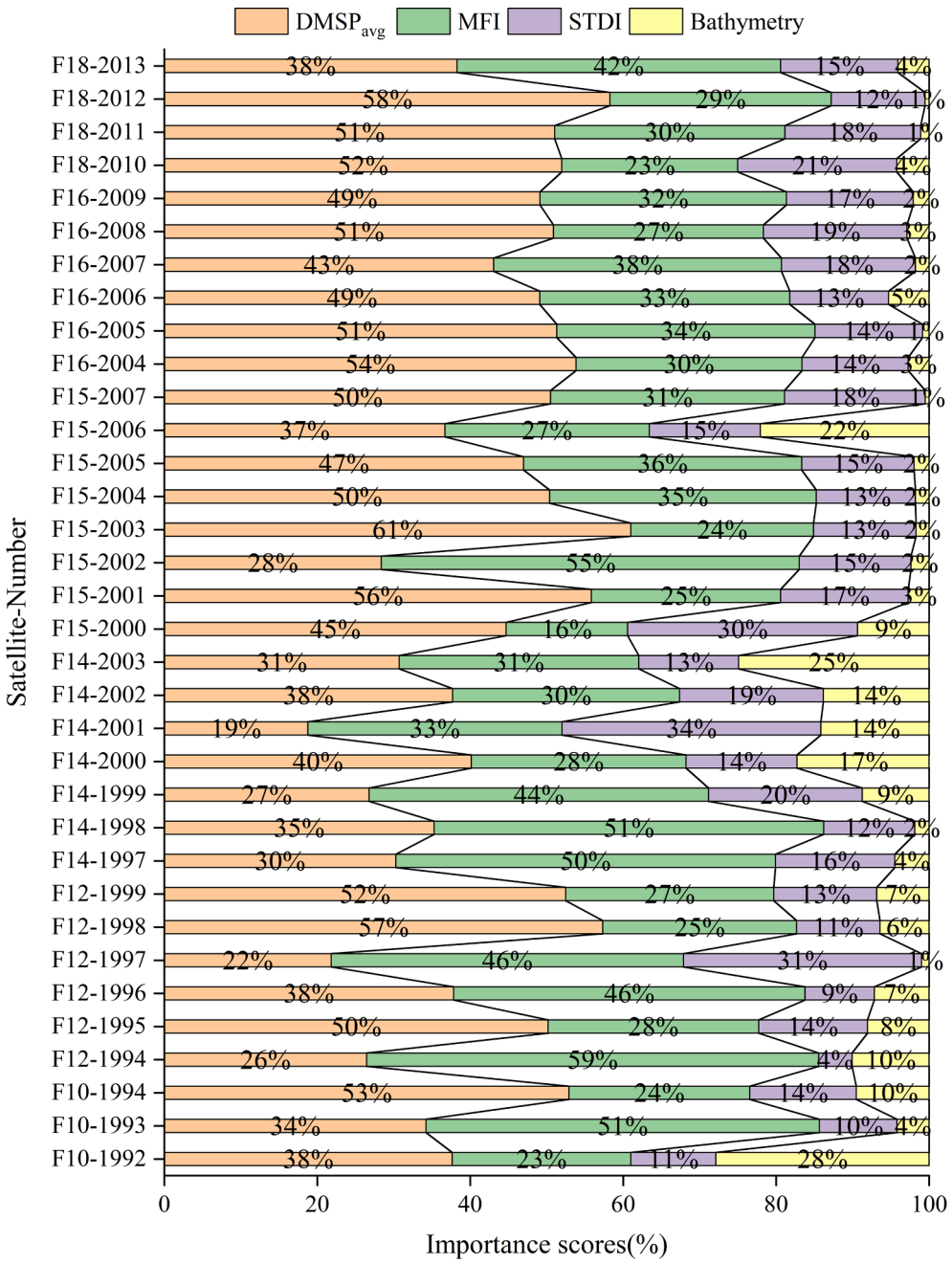

Fig. 9. Importance scores of the composite images used in the RF denoise approach.

functions are listed in Table 2.

3.3. Performance assessment of the intercalibration

The TLIs derived from the original DMSP$_{avg}$ (avg_TLIs), DMSP$_{avg}$ denoised using RF (RF_TLIs), and DMSP$_{avg}$ denoised using TS (TS_TLIs) are presented in Fig. 11a and 11b. When compared with avg_TLIs, both the RF_TLIs and TS_TLIs were significantly reduced. This may be because massive noise pixels were removed using the RF or TS methods.

As shown in Fig. 11b, the trajectories of RF_TLIs and TS_TLIs were similar. The TLIs of F12 were higher than those values for F10 and F14. The TLIs of F15 were divided into two stages: 1) the TLIs remained at the same level as F12 from 2000 to 2002, and 2) the TLIs remained at the same level as F14 from 2003 to 2007. The TLIs of F18 were higher than those of the previous satellites. Similar TLI trajectories have also been observed in inland NTL stable images (Li and Zhou 2017). In addition, the RF_TLIs were observed to be commonly higher than the TS_TLIs. This was because more effective pixels were mistakenly removed using the TS method.

To investigate the contribution of RF in the intercalibration, the same stepwise intercalibration model was applied to the TS denoised images. The RF_TLIs and TS_TLIs after stepwise intercalibration (RF$_{cal}$_TLIs and TS$_{cal}$_TLIs) are shown in Fig. 11c. The RF_TLIs intercalibrated using the PIFs method proposed by Elvidge et al. (2011) and Elvidge et al. (2014) are shown in Fig. 11c using orange lines. As seen in the figure, the biases of the RF_TLIs were better eliminated by the proposed method (RF$_{cal}$_TLIs) than those of the TS$_{cal}$_TLIs for most of the years studied. Specifically, the biases of the TS$_{cal}$_TLIs were not adequately reduced between F10 and F12 during 1994 and between F12 and F14 from 1997 to 1999.

The RF$_{cal}$_TLIs intercalibrated by the PIFs method proposed by Elvidge et al. (2011) and Elvidge et al. (2014) were shown to be more

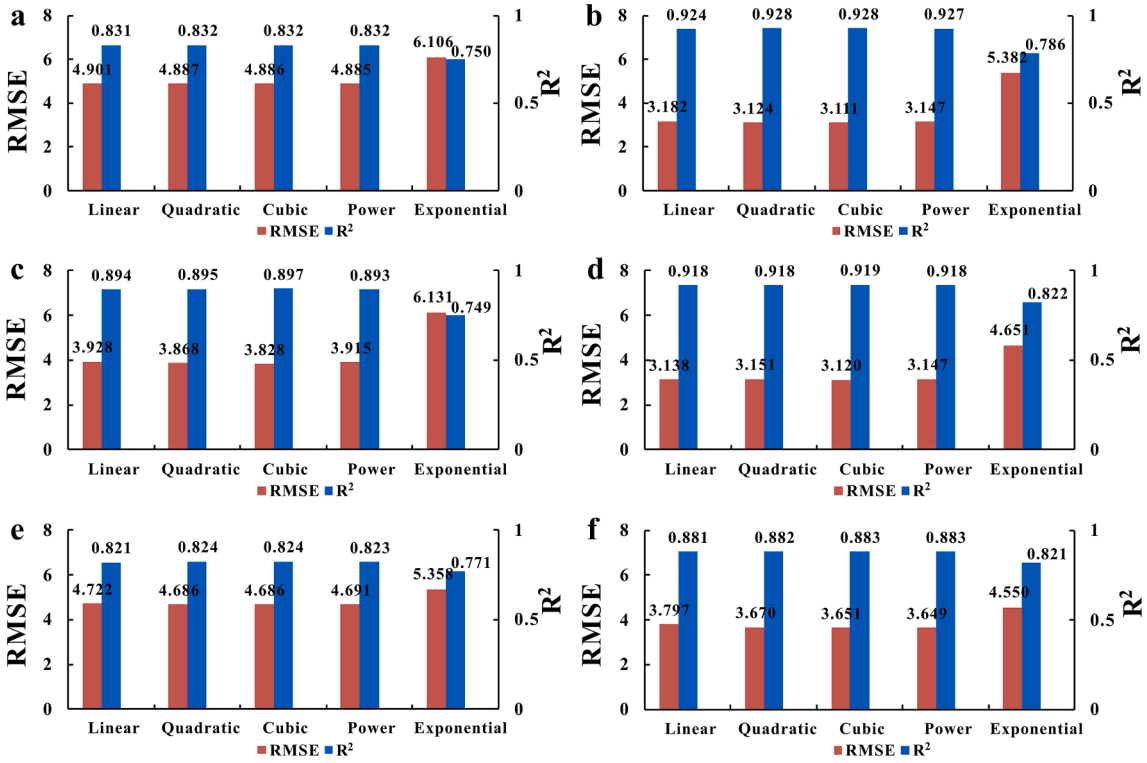

Fig. 10. Average R^2 and average RMSE corresponding to each candidate pending function for step 1 (a), step 2 (b), step 3 (c), step 4 (d), step 5 (e), and step 6 (f) of the intercalibration.

Table 2
List of the best fitting functions and their respective coefficients.

Step	function	Coefficients
1	Eq. (4)	k = 1.555, l = 0.8832, m = 1.091
2	Eq. (3)	g = -0.0001081, h = 0.004975,i = 1.082, j = 1.397
3	Eq. (3)	g = -0.0002234, h = 0.01403, i = 0.933, j = 2.804
4	Eq. (3)	g = -0.0001526, h = 0.01247, i = 0.7435, j = 3.105
5	Eq. (3)	g = 7.496e-05, h = -0.002692, i = 0.7968, j = 0.6883
6	Eq. (4)	k = 1.013, l = 0.9969, m = -0.05397

consistent than the proposed method. However, the upward trend of the RF_{cal}_TLIs intercalibrated by the PIFs method proposed by Elvidge et al. (2014) is not as significant as the RF_{cal}_TLIs intercalibrated by using the proposed method. In addition, there was an abnormally rapid increase from 2010 to 2013 for the RF_{cal}_TLIs intercalibrated using the PIFs method. This implies that the PIFs method may not be suitable for NTL intercalibration in ocean areas.

To further quantitatively assess the consistency, SNDIs of the original $DMSP_{avg}$ ($SNDI_{avg}$), $DMSP_{avg}$ denoised using the TS method ($SNDI_{TS}$), $DMSP_{avg}$ denoised using the RF approach ($SNDI_{RF}$), $SNDI_{TS}$ and $SNDI_{RF}$ after stepwise intercalibration ($SNDI_{TS\_cal}$ and $SNDI_{RF\_cal(proposed)}$), and $SNDI_{RF}$ after PIFs intercalibration ($SNDI_{RF\_cal(Elvidge)}$) are shown in Fig. 12. The $SNDI_{RF}$ is usually less than the $SNDI_{TS}$, e.g. the $SNDI_{RF}$ of the study area was 16.8% less than that of $SNDI_{TS}$.

However, $SNDI_{avg}$ was lower than both $SNDI_{RF}$ and $SNDI_{TS}$. This does not mean that the biases become larger after the RF or TS denoising approaches. In fact, there were a large number of noise pixels in the original $DMSP_{avg}$, so the TLIs of the original $DMSP_{avg}$ were much larger than those of the RF or TS denoised pixels, as shown in Fig. 12. In this case, $SNDI_{avg}$ can also become abnormally low because of massive noise according to Eq. (7) and Eq. (8).

After the stepwise intercalibration, both $SNDI_{RF\_cal}$ and $SNDI_{TS\_cal}$ were much lower than the $SNDI_{avg}$, e.g., for the whole study area, $SNDI_{RF\_cal}$ was 68.2% less than $SNDI_{avg}$, and $SNDI_{TS\_cal}$ was 38.2% less than $SNDI_{avg}$. $SNDI_{RF\_cal(Elvidge)}$ had the lowest SNDI. However, the high consistency may stem from the overly flat TLI trend described in the preceding paragraph. This indicates that the proposed method may be more appropriate for ocean areas than the PIF method. This is discussed further in the following section.

Furthermore, pixel_$SNDI_{RF_cal}$ (pixel_SNDI after RF denoising and stepwise intercalibration) was 1.098, which was 32.2% less than pixel_$SNDI_{avg}$ (pixel_SNDI of the original $DMSP_{avg}$). This is also an important auxiliary evidence that the proposed method can effectively reduce radiometric biases in ocean areas.

4. Discussions

4.1. Features such as MFI, STDI, and bathymetric data increased the RF denoising

Owing to the diffusion effect, the effective pixels have a structure that is blurred rather than isolated highlight points, as shown in Fig. 13f and g. MFI and STDI can help the RF to distinguish the blurred structures from the isolated highlight points in the proposed method. On the one hand, as shown in Fig. 13c, d, f, and g, some effective pixels distributed at the edges of the blurring structures were discarded by the TS approach. By contrast, such effective pixels can be successfully

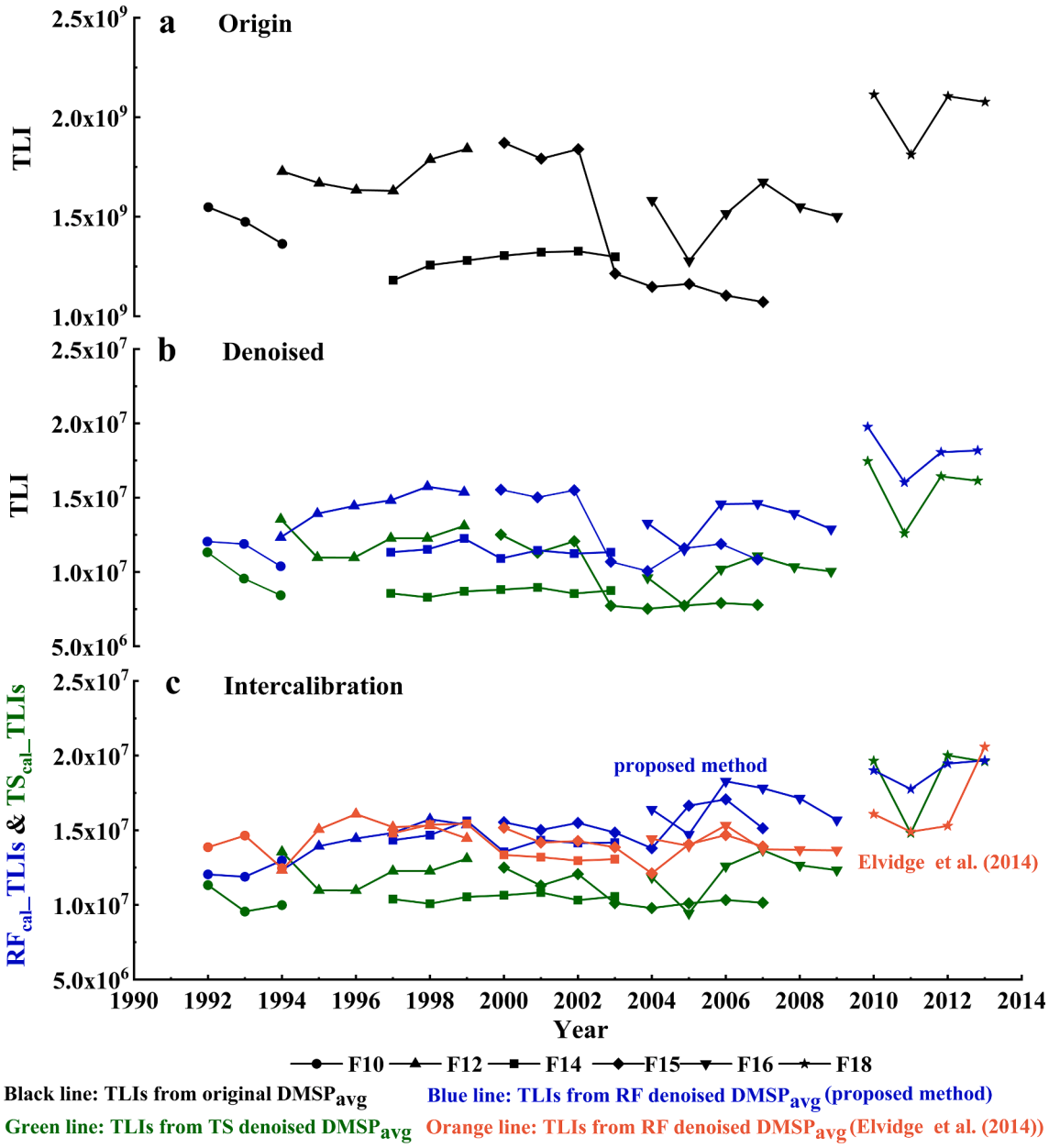

Fig. 11. Time series TLIs derived from the original $DMSP_{avg}$ (a), time series TLIs derived from corresponding images denoised by using the RF (blue line) and the TS (green line) respectively (b), time series TLIs derived from corresponding images intercalibrated using the proposed method (blue line), TS method (green line), and PIFs method proposed by Elvidge et al. (2014) (orange line) (c). (For interpretation of the references to colour in this figure legend, the reader is referred to the web version of this article.)

preserved using the proposed method. On the other hand, the sum of the average RF importance scores of MFI and STDI was even greater than that of $DMSP_{avg}$, as shown in Fig. 9.

Furthermore, the quality of $DMSP_{avg}$ is worse in middle-high latitude areas than in low latitude areas, for example, the DN values of some noise pixels in middle to high latitude areas are much higher than in the low-latitude areas (Pandey et al., 2017; Wu et al., 2013). Therefore, many noise pixels were misidentified as effective pixels during the TS approach, but they were not misclassified using the proposed method, as shown in Fig. 13b and e.

Despite the bathymetric data showing the lowest average importance score (7%), a part of importance scores of the bathymetric data were significantly higher than the average as shown in Fig. 9, such as F10-1992 (28%), F14-2000–2003 (14%, 17%, 14%, 25%). Coincidently, the TLIs of these images were much higher than those of the other images which were captured by the same satellite, as shown in Fig. 11a. The TLIs of those images and their differences from the other images captured by the same satellite were both found to have decreased, as shown in Fig. 11b. We assumed that the TLIs of those images were overestimated, and that the bathymetric data may be able to increase the RF denoising when the TLI is overestimated.

In summary, RF denoising can be increased by combining the MFI, STDI, and bathymetric data with the original $DMSP_{avg}$. We believe that this is an important reason why the proposed stepwise intercalibration method was able to effectively reduce systematic radiometric biases.

4.2. Correlation between the TLIs and fishery catches as a supplement to confirm the effectiveness of the proposed method

The EEZs of Japan and Malaysia were selected to illustrate the

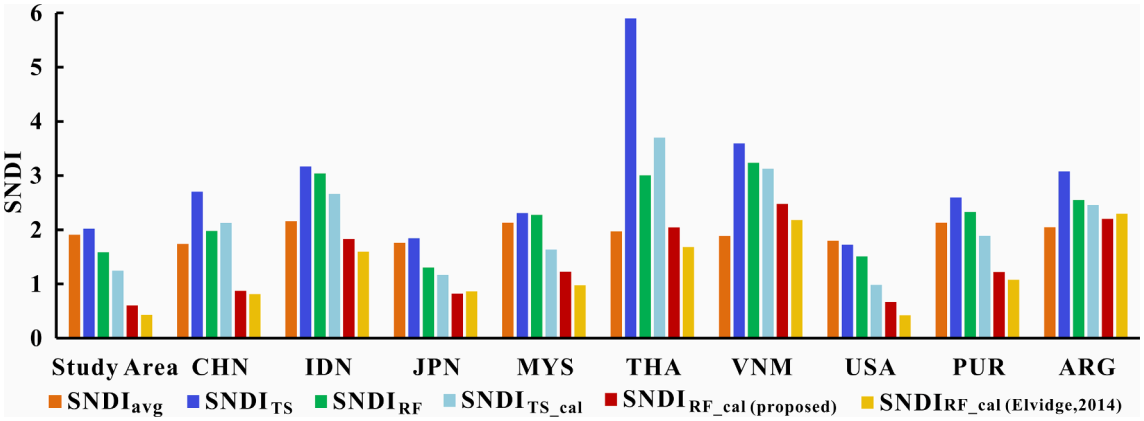

Fig. 12. SNDI derived from the raw DMSP image, TS denoised image, and RF denoised image before and after calibration for the whole study area and several EEZs.

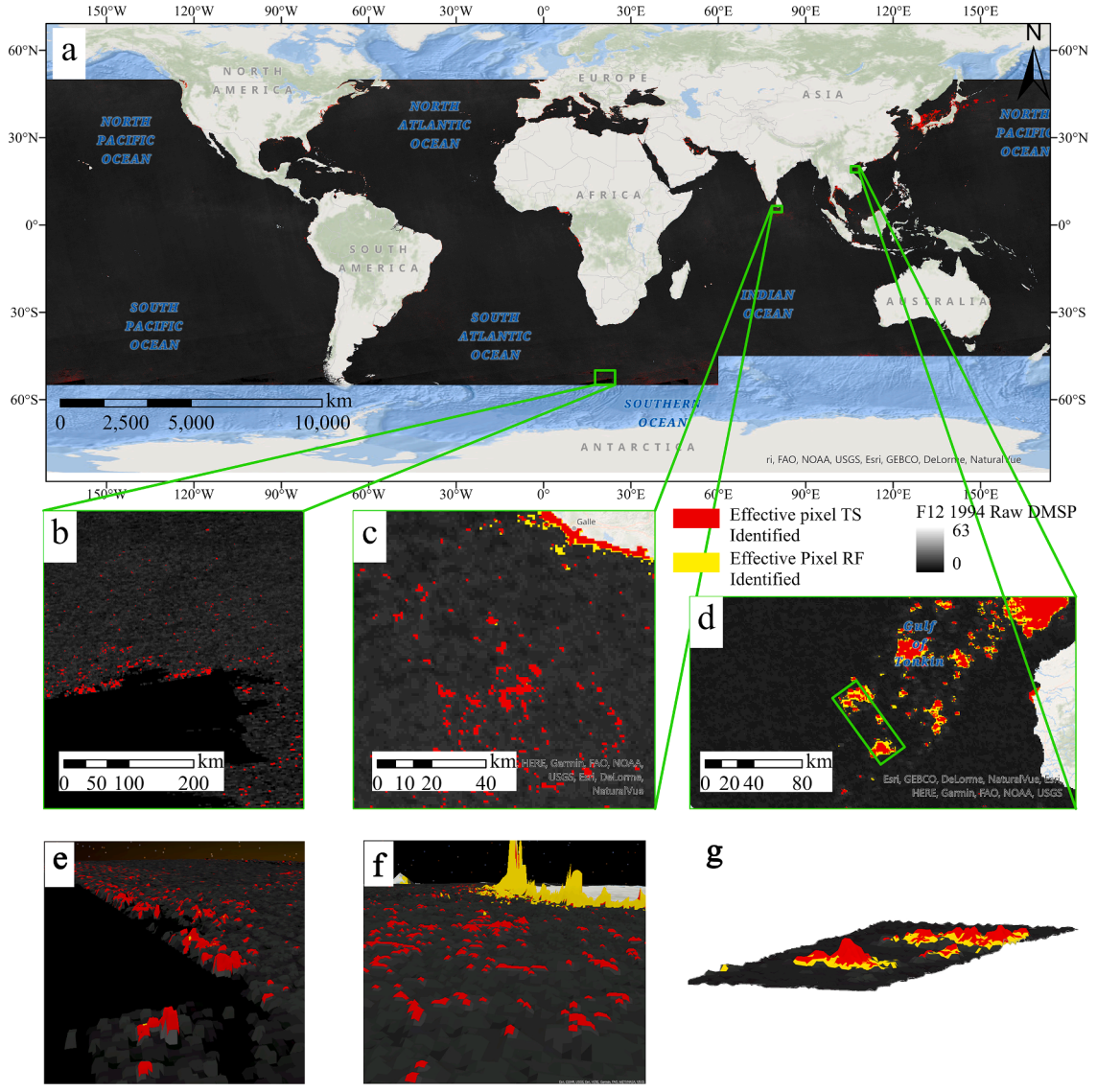

Fig. 13. Schematic of $DMSP_{avg}$ overlaid with images of effective pixels identified by RF and TS (a) and zoomed–in for middle to high latitude area (b), low latitude area (c), deep-sea fishing vessels (d) and the corresponding stereoscopic images for middle-high latitude area (e), low latitude area (f). The green squares in (d) is the location of the pixel shown in stereoscopic images (g). The height for pixels in stereoscopic images were built by DN values. (For interpretation of the references to colour in this figure legend, the reader is referred to the web version of this article.)

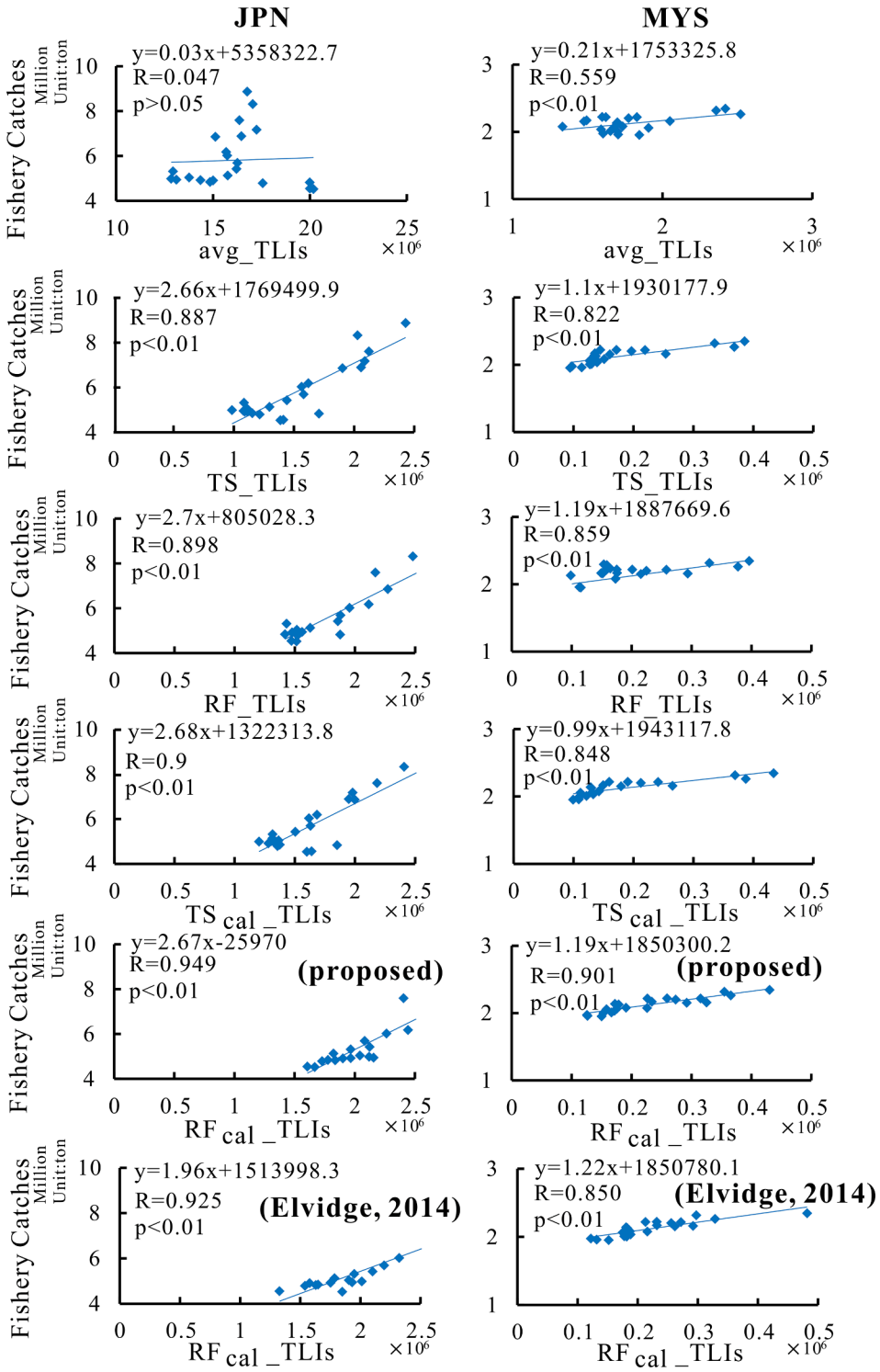

Fig. 14. Correlation coefficients between the TLIs and fishery catches of both Japan and Malaysia.

effectiveness of the proposed method. They were chosen because their fishery resources have an opposite development trend; that is, the fishery development trend of Japan tends to be gradually declining, while that of Malaysia tends to steadily increasing.

The correlations between TLIs and fishery catches for Japan and Malaysia are shown in Fig. 14. The correlation coefficients between the avg_TLIs and the fishery catches were the lowest for both EEZs, and the correlation coefficients between the RF_{cal}_TLIs derived from the proposed method and the fishery catches were shown to be the highest.

In addition, the correlation coefficients between the fishery catches and the RF_TLIs derived from the data intercalibrated by using PIFs proposed by Elvidge et al. (2014) are lower than that between the RF_{cal}_TLIs (proposed) and fishery catches.

These results provide additional evidence to prove the effectiveness of the stepwise intercalibration with RF denoising, that is, the proposed method can reduce the systematic radiometric biases effectively and also enhance the RF_{cal}_TLIs as an indicator of human activities in the marine environment. This is also an important reason why we have previously

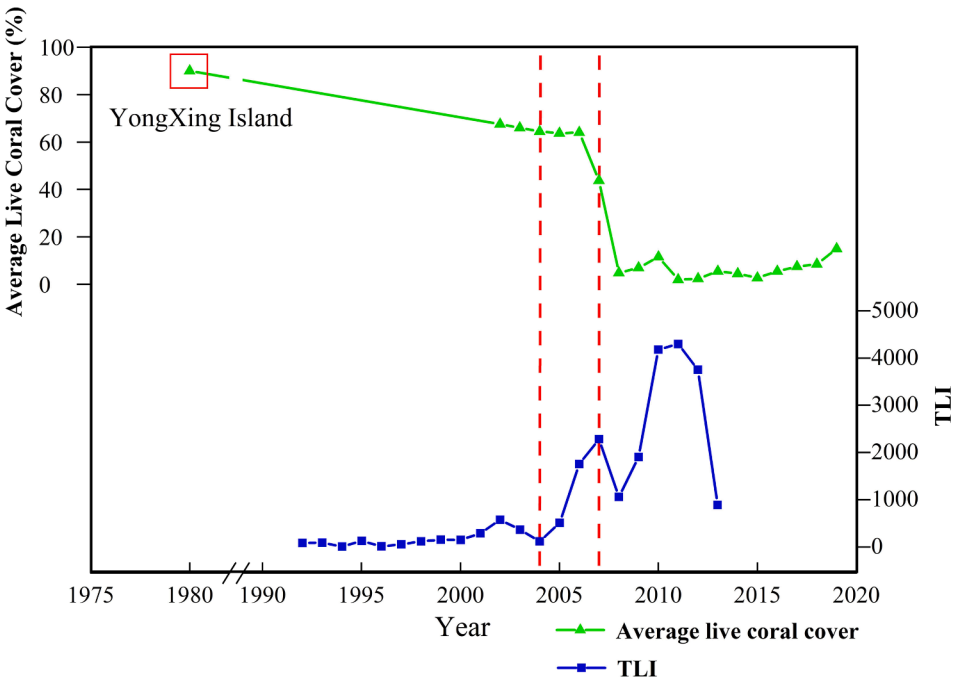

Fig. 15. Comparison between the TLIs and the live coral covers in Xisha Islands, South China Sea: live coral covers are come from Li et al. (2019) and Yu (2012). The live coral cover is seen to be drastically declined during 2006 to 2008, which is just about 3 years after the TLI begins to increase significantly; and the live coral cover seems to recover after the TLI starts to rapidly decrease. More discussions on the relationship between the TLIs and the live coral covers need us to further span the time series NTL data as long as possible in future work.

stated that the proposed method may be more appropriate for ocean areas than the PIF method, although $SNDI_{RF\_cal(Elvidge)}$ was found to be the lowest.

4.3. Potential applications and future improvements

As the TLIs are well correlated with fishery catches, so the consistent time series NTL data has a great potential to be used to discuss on the variations of the carbon emissions with the ocean human activities, the development of ocean economy, or the influences of human activities on the changes of the ocean ecosystem such as coral reefs in a large scale. For example, as shown in Fig. 15, the consistent time series NTL data provide a first comparison between human activities (TLIs) and the average live coral covers in South China Sea (SCS). In other word, it makes quantitative and semi-quantitative analysis on how human activities effect on the global degradation of coral reefs become possible.

However, as can be seen from Fig. 15, the consistent NTL time series spanned only from 1992 to 2013. Some researchers have intercalibrated the DMSP-OLS and NPP-VIIRS data for a long-term (2000 to 2018) analysis on non-oceanic area (Chen et al., 2020; Nechaev et al., 2021; Tilottama et al., 2021). As a result, it is still necessary in future to combine the proposed intercalibration with the cross-sensor calibration proposed by Chen et al. (2020), Nechaev et al. (2021), and Tilottama et al. (2021), or directly extend the proposed intercalibration to a cross-intercalibration between the DMSP-OLS and NPP-VIIRS data in a large-scale oceanic area for spanning the time series NTL data as long as possible (1992 to current).

Finally, note that there are many other machine learning algorithms such as Neural Network (NN) and Support Vector Machine (SVM) could potentially be applied to the denoising approach. Hence, another important task in future work is to further assess the performances of those intercalibration approaches that make use of other machine learning algorithms such as NN and SVM instead of the RF in the proposed method.

5. Conclusions

To evaluate human activities for ocean ecosystem research and application, this study provides a method to generate a consistent NTL time series for a large-scale oceanic area from the $DMSP_{avg}$. The main idea of this study was to combine an RF approach with stepwise intercalibration. Specifically, the noise that impeded the stepwise intercalibration was first removed using an RF approach. Here, a feature image composited by the original $DMSP_{avg}$, MFI, STDI, and bathymetric data was utilized to increase RF denoising. Thereafter, stepwise intercalibration is implemented on the denoised DMSP images to reduce the systematic radiometric biases.

Experimental results showed that the composite image can increase RF denoising and help eliminate systematic radiometric biases during stepwise intercalibration. The overall accuracy and Kappa coefficient of the RF approach reached 96% and 0.775, respectively. Based on RF denoising, the systematic radiometric biases of the $DMSP_{avg}$ were found to be significantly reduced by stepwise intercalibration, that is, the SNDI of the images calibrated using the proposed method can reach 0.61, which is 68.2% less than that of the original $DMSP_{avg}$. Furthermore, the effectiveness of the proposed method was confirmed by using the correlation coefficients between the TLIs and the fishery catch data, that is, the correlation coefficients between the TLIs derived from the images calibrated using the proposed method and fishery catches of Japan and Malaysia can reach 0.949 and 0.901, respectively, which is the highest compared to others, including the TS and PIF methods. This implies that the TLIs can be used as effective indicators of fishery activities for ocean ecosystem research such as the discussions on the global coral reef degradations, and for other various applications such as the estimation of human-activity-caused ocean carbon emission changes in the future.

In summary, the proposed method proved to be accurate, effective, and feasible for generating consistent time-series NTL data for large-scale ocean areas. Compared to current open access dataset, the produced consistent time series NTL data is specialized for the oceanic

areas, which will be helpful for the studies and practices of ocean ecosystems and large-scale ocean human activities.

CRediT authorship contribution statement

Rongyong Huang: Conceptualization, Methodology, Supervision, Writing – review & editing, Funding acquisition. **Wenqian Wu:** Writing – original draft, Conceptualization, Methodology, Software, Data curation, Visualization, Writing – review & editing. **Kefu Yu:** Writing – review & editing, Resources, Supervision, Project administration, Funding acquisition.

Declaration of Competing Interest

The authors declare that they have no known competing financial interests or personal relationships that could have appeared to influence the work reported in this paper.

Acknowledgments

This research is supported by National Natural Science Foundation of China (Nos. 42090041, 42030502, 41766007), Guangxi Science and Technology Project (Nos. AD17129063, AA17204074), Natural Sciences Foundation of Guangxi, China (No. 2020GXNSFAA297245), and Self-Topic Project of Guangxi Laboratory on the Study of Coral Reefs in the South China Sea, Nanning 530004, China (No. GXLSCRSCS2021102). Special thanks are given to the anonymous reviewers and members of the editorial board for their suggestions of improving this article. We also appreciate for NGDC (https://www.ngdc.noaa.gov/eog/download.html), FAO (http://www.fao.org/fishery/area), Maritime Boundaries (https://www.marineregions.org),v GEBCO (https://www.gebco.net/data_and_products), and Sea Around Us (http://www.seaaroundus.org) for providing the DMSP/OLS NTL images, the MFA boundaries data, the EEZs boundaries, the bathymetry data, and the Fishery catches data, respectively.

Appendix A

See Fig. A1.
See Table A1.

Table A1
Time distribution and numbering of DMSP/OLS night-time light datasets for different satellites.

Year/ Satellite	F10	F12	F14	F15	F16	F18
1992	F10-1992	–	–	–	–	–
1993	F10-1993	–	–	–	–	–
1994	F10-1994	F12-1994	–	–	–	–
1995	–	F12-1995	–	–	–	–
1996	–	F12-1996	–	–	–	–
1997	–	F12-1997	F14-1997	–	–	–
1998	–	F12-1998	F14-1998	–	–	–
1999	–	F12-1999	F14-1999	–	–	–
2000	–	–	F14-2000	F15-2000	–	–
2001	–	–	F14-2001	F15-2001	–	–
2002	–	–	F14-2002	F15-2002	–	–
2003	–	–	F14-2003	F15-2003	–	–
2004	–	–	–	F15-2004	F16-2004	–
2005	–	–	–	F15-2005	F16-2005	–
2006	–	–	–	F15-2006	F16-2006	–
2007	–	–	–	F15-2007	F16-2007	–
2008	–	–	–	–	F16-2008	–
2009	–	–	–	–	F16-2009	–
2010	–	–	–	–	–	F18-2010
2011	–	–	–	–	–	F18-2011
2012	–	–	–	–	–	F18-2012
2013	–	–	–	–	–	F18-2013

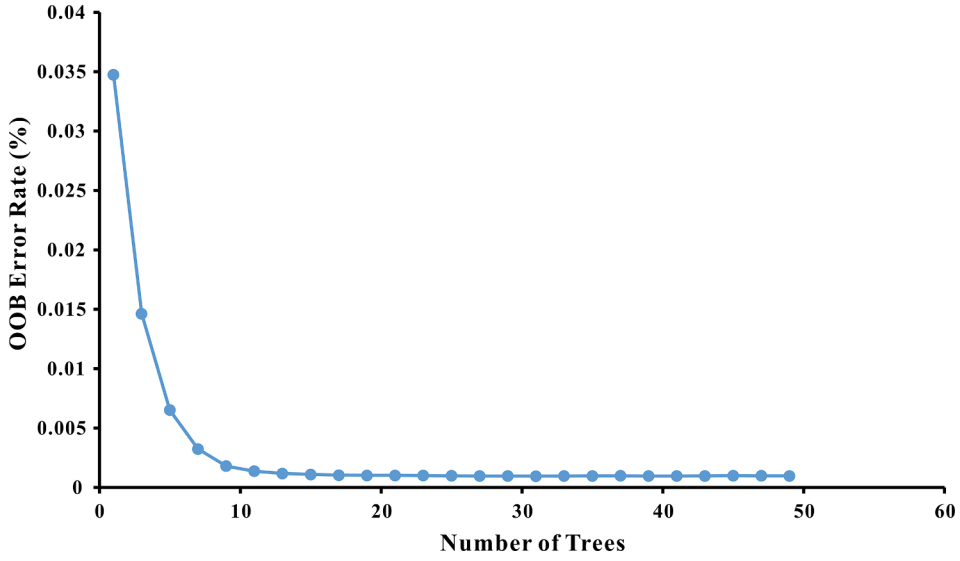

Fig. A1. OOB Error rates with number of trees.

References

Aubrecht, C., Elvidge, C.D., Longcore, T., Rich, C., Safran, J., Strong, A.E., Eakin, C.M., Baugh, K.E., Tuttle, B.T., Howard, A.T., Erwin, E.H., 2008. A global inventory of coral reef stressors based on satellite observed nighttime lights. Geocarto Int 23, 467–479.

Breiman, L., 2001. Random Forests. Mach. Learn. 45, 5–32.

Chen, X., Yu, K., Huang, X., Wang, Y., Liao, Z., Zhang, R., Yao, Q., Wang, J., Wang, W., Tao, S., Zhang, H., 2019. Atmospheric Nitrogen Deposition Increases the Possibility of Macroalgal Dominance on Remote Coral Reefs. J. Geophys. Res.-Biogeo. 124, 1355–1369.

Chen, Z., Yu, B., Yang, C., Zhou, Y., Qian, X., Wang, C., Wu, B., Wu, J., 2020. An extended time-series (2000–2018) of global NPP-VIIRS-like nighttime light data from a cross-sensor calibration. Earth Syst. Sci. Data Discuss 1–34.

Chen, Y.p., Wei, Y.q., Peng, L.H., 2018. Ecological technology model and path of seaport reclamation construction. Ocean Coast Manage. 165, 244–257.

Cheng, Y., Zhao, L., Wan, W., Li, L., Yu, T., Gu, X., 2016. Extracting urban areas in China using DMSP/OLS nighttime light data integrated with biophysical composition information. J. Geog. Sci. 26, 325–338.

Cheng, T., Zhou, W., Xu, H., Fan, W., 2017. Estimation of Fishing Vessel Numbers Close to the Terminator in the Pacific Northwest Using OLS/DMSP Data. Geo-Spatial Knowl. Intell. 321–327.

Croft, T., 1978. Nighttime Images of the Earth from Space. Sci. Am. - SCI AMER 239, 86–98.

D'Angelo, C., Wiedenmann, J., 2014. Impacts of nutrient enrichment on coral reefs: new perspectives and implications for coastal management and reef survival. Curr. Opin. Env. Sust. 7, 82–93.

Derrick, B., Noranarttragoon, P., Zeller, D., Teh, L.C.L., Pauly, D., 2017. Thailand's Missing Marine Fisheries Catch (1950–2014). Front. Mar. Sci. 4, 402.

Elvidge, C.D., Baugh, K.E., Kihn, E.A., Kroehl, H.W., Davis, E.R., Davis, C.W., 1997. Relation between satellite observed visible-near infrared emissions, population, economic activity and electric power consumption. Int. J. Remote Sens. 18, 1373–1379.

Elvidge, C., Baugh, K., Zhizhin, M., Hsu, F.-C., 2013. Why VIIRS data are superior to DMSP for mapping nighttime lights. Proceedings of the Asia-Pacific Advanced Network 35, 62–69.

Elvidge, C.D., Ziskin, D., Baugh, K.E., Tuttle, B.T., Ghosh, T., Pack, D.W., Erwin, E.H., Zhizhin, M., 2009. A Fifteen Year Record of Global Natural Gas Flaring Derived from Satellite Data. Energies 2, 595–622.

Elvidge, C.D., Sutton, P.C., Baugh, K.E., Ziskin, D., Tilottama, G., Anderson, S., 2011. National Trends in Satellite Observed Lighting: 1992–2009. AGU Fall Meeting Abstracts 3, 03.

Elvidge, C.D., Hsu, F.-C., Baugh, K.E., Ghosh, T., 2014. National trends in satellite-observed lighting. Global Urban Monitor. Assess. Through Earth Observ. 23, 97–118.

Elvidge, C.D., Zhizhin, M., Baugh, K., Hsu, F.-C., 2015. Automatic Boat Identification System for VIIRS Low Light Imaging Data. Remote Sens. 7, 3020–3036.

Elvidge, C.D., Ghosh, T., Baugh, K., Zhizhin, M., Hsu, F.-C., Katada, N.S., Penalosa, W., Hung, B.Q., 2018. Rating the Effectiveness of Fishery Closures With Visible Infrared Imaging Radiometer Suite Boat Detection Data. Front. Mar. Sci. 5, 132.

Gissi, E., Manea, E., Mazaris, A.D., Fraschetti, S., Almpanidou, V., Bevilacqua, S., Coll, M., Guarnieri, G., Lloret-Lloret, E., Pascual, M., Petza, D., Rilov, G., Schonwald, M., Stelzenmuller, V., Katsanevakis, S., 2021. A review of the combined effects of climate change and other local human stressors on the marine environment. Sci. Total Environ. 755, 142564.

Golden, C.D., Allison, E.H., Cheung, W.W.L., Dey, M.M., Halpern, B.S., McCauley, D.J., Smith, M., Vaitla, B., Zeller, D., Myers, S.S., 2016. Nutrition: Fall in fish catch threatens human health. Nature 534, 317–320.

Guo, G., Fan, W., Xue, J., Zhang, S., Zhang, H., Tang, F., Cheng, T., 2017. Identification for operating pelagic light-fishing vessels based on NPP/VIIRS low light imaging data. Nongye Gongcheng Xuebao/Trans. Chin. Soc. Agric. Eng. 33, 245–251.

Hu, S., Ge, Y., Liu, M., Ren, Z., Zhang, X., 2022. Village-level poverty identification using machine learning, high-resolution images, and geospatial data. Int. J. Appl. Earth Obs. 107, 102694.

Huang, R., Zhang, H., Yu, K., 2019. Analysis on the Live Coral Cover around Weizhou Island Using MODIS Data. Sensors 19.

Jenssen, B.M., 1996. An overview of exposure to, and effects of, petroleum oil and organochlorine pollution in grey seals (Halichoerus grypus). Sci. Total Environ. 186, 109–118.

Jin, X., Long, Y., Sun, W., Lu, Y., Yang, X., Tang, J., 2017. Evaluating cities' vitality and identifying ghost cities in China with emerging geographical data. Cities 63, 98–109.

Jin, H., Mountrakis, G., Stehman, S.V., 2014. Assessing integration of intensity, polarimetric scattering, interferometric coherence and spatial texture metrics in PALSAR-derived land cover classification. Isprs J. Photogramm. 98, 70–84.

Kedia, A.C., Kapos, B., Liao, S., Draper, J., Eddinger, J., Updike, C., Frazier, A.E., 2021. An Integrated Spectral-Structural Workflow for Invasive Vegetation Mapping in an Arid Region Using Drones. Drones 5, 19.

Kiyofuji, H., Saitoh, S.-I., 2004. Use of nighttime visible images to detect Japanese common squid Todarodes pacificus fishing areas and potential migration routes in the Sea of Japan. Mar. Ecol.-Progr. Ser. 276, 173–186.

Kroodsma, D., Mayorga, J., Hochberg, T., Miller, N., Boerder, K., Ferretti, F., Wilson, A., Bergman, B., White, T., Block, B., Woods, P., Sullivan, B., Costello, C., Worm, B., 2018. Tracking the Global Footprint of Fisheries. Science 359.

Li, Y., Yu, K., Wang, Y., Guo, J., Huang, X., Pei, J., Luo, Y., 2017b. Distribution Characteristics of Surface Seawater Nutrients in Summer around Luhuitou Reef in Sanya. Trop. Geogr. 37, 708–717.

Li, Y., Wu, Z., Liang, J., Chen, S., Zhao, J., 2019. Analysis on the outbreak period and cause of Acanthaster planci in Xisha Islands in recent 15 years (in Chinese). Chin. Sci. Bull. 64, 3478–3484.

Li, D., Zhao, X., Li, X., 2016. Remote sensing of human beings – a perspective from nighttime light. Geo-spat. Inform. Sci. 19, 69–79.

Li, X., Zhou, Y., 2017. A Stepwise Calibration of Global DMSP/OLS Stable Nighttime Light Data (1992–2013). Remote Sens.-Basel 9, 637.

Li, X., Li, D., Xu, H., Wu, C., 2017a. Intercalibration between DMSP/OLS and VIIRS night-time light images to evaluate city light dynamics of Syria's major human settlement during Syrian Civil War. Int. J. Remote Sens. 38, 5934–5951.

Liang, L., Bian, J., Li, A., Feng, W., Lei, G., Zhang, Z., Zuo, J., 2019. Consistent intercalibration of nighttime light data between DMSP/OLS and NPP/VIIRS in the China–Pakistan Economic Corridor. IGARSS 2019 - 2019 IEEE International Geoscience and Remote Sensing Symposium 24, 149–160.

Liu, Y., Delahunty, T., Zhao, N., Cao, G., 2016. These lit areas are undeveloped: Delimiting China's urban extents from thresholded nighttime light imagery. Int. J. Appl. Earth Obs. 50, 39–50.

Liu, Z., He, C., Zhang, Q., Huang, Q., Yang, Y., 2012. Extracting the dynamics of urban expansion in China using DMSP-OLS nighttime light data from 1992 to 2008. Landscape Urban Plann. 106, 62–72.

Liu, J., Huang, R., Yu, K., 2020a. Analysis on the geomorphic changes of Huangyan Island based on satellite images over the past 40 years. Quarter. Sci. 40, 775–790.

Liu, J., Huang, R., Yu, K., Zou, B., 2020b. How lime-sand islands in the South China Sea have responded to global warming over the last 30 years: Evidence from satellite remote sensing images. Geomorphology 371, 107423.

Lu, W., Liu, Y., Wang, J., Xu, W., Wu, W., Liu, Y., Zhao, B., Li, H., Li, P., 2020. Global proliferation of offshore gas flaring areas. J. Maps 16, 396–404.

Maxwell, M.R., Henry, A., Elvidge, C.D., Safran, J., Hobson, V., Nelson, I., Tuttle, B., Dietz, J., Hunter, J., 2004. Fishery dynamics of the California market squid (Loligo opalescens), as measured by satellite remote sensing. Fish B-Noaa 102, 661–670.

Nechaev, D., Zhizhin, M., Poyda, A., Ghosh, T., Hsu, F.-C., Elvidge, C., 2021. Cross-Sensor Nighttime Lights Image Calibration for DMSP/OLS and SNPP/VIIRS with Residual U-Net. Remote Sens.-Basel 13, 5026.

Pandey, B., Zhang, Q., Seto, K.C., 2017. Comparative evaluation of relative calibration methods for DMSP/OLS nighttime lights. Remote Sens. Environ. 195, 67–78.

Puttanapong, N., Martinez, A., Bulan, J.A.N., Addawe, M., Durante, R.L., Martillan, M., 2022. Predicting Poverty Using Geospatial Data in Thailand. Isprs. Int. Geo-Inf. 11, 293.

Robards, M., Silber, G., Adams, J., Arroyo, J., Lorenzini, D., Schwehr, K., Amos, J., 2016. Conservation science and policy applications of the marine vessel Automatic Identification System (AIS)-A review. Bull. Mar. Sci. -Miami- 92, 75–103.

Rodhouse, P.G., Elvidge, C.D., Trathan, P.N., 2001. Remote sensing of the global light-fishing fleet: An analysis of interactions with oceanography, other fisheries and predators. Adv. Mar. Biol. 39, 261–303.

Ruiz, J., Caballero, I., Navarro, G., 2020. Sensing the Same Fishing Fleet with AIS and VIIRS: A Seven-Year Assessment of Squid Jiggers in FAO Major Fishing Area 41. Remote Sens. 12, 32.

Saitoh, S.-I., Fukaya, A., Saitoh, K., Semedi, B., Mugo, R., Matsumura, S., Fumihiro, T., 2010. Estimation of number of pacific saury fishing vessels using night-time visible images. ISPRS Commision VIII, XXXVIII Part, p. 8.

Shi, K., Chen, Y., Yu, B., Xu, T., Yang, C., Li, L., Huang, C., Chen, Z., Liu, R., Wu, J., 2016. Detecting spatiotemporal dynamics of global electric power consumption using DMSP-OLS nighttime stable light data. Appl. Energy 184, 450–463.

Shi, F., Li, X., Xu, H., 2017. Analysis of Human Activities in Nature Reserves Based on Nighttime Light Remote Sensing and Microblogging Data –Illustrated by the Case of National Nature Reserves in Jiangxi Province. ISPRS – Int. Arch. Photogramm., Remote Sens. Spat. Inf. Sci. XLII-2/W7, 1341–1348.

Stefanski, J., Mack, B., Waske, B., 2013. Optimization of Object-Based Image Analysis With Random Forests for Land Cover Mapping. Ieee J.-Stars 6, 2492–2504.

Tian, F., Wu, B., Zeng, H., Watmough, G.R., Zhang, M., Li, Y., 2022. Detecting the linkage between arable land use and poverty using machine learning methods at global perspective. Geogr. Sustain. 3, 7–20.

Tilottama, G., Baugh, K., Elvidge, C., Zhizhin, M., Poyda, A., Hsu, F.-C., 2021. Extending the DMSP Nighttime Lights Time Series beyond 2013. Remote Sens.-Basel 13, 5004.

Waluda, C.M., Yamashiro, C., Elvidge, C.D., Hobson, V.R., Rodhouse, P.G., 2004. Quantifying light-fishing for Dosidicus gigas in the eastern Pacific using satellite remote sensing. Remote Sens. Environ. 91, 129–133.

Waluda, C.M., Griffiths, H.J., Rodhouse, P.G., 2008. Remotely sensed spatial dynamics of the Illex argentinus fishery, Southwest Atlantic. Fish Res. 91, 196–202.

Waluda, C.M., Trathan, P.N., Elvidge, C.D., Hobson, V.R., Rodhouse, P.G., 2011. Throwing light on straddling stocks of Illex argentinus: Assessing fishing intensity with satellite imagery. Can. J. Fish Aquat. Sci. 59, 592–596.
Wu, J., He, S., Peng, J., Li, W., Zhong, X., 2013. Intercalibration of DMSP-OLS night-time light data by the invariant region method. Int. J. Remote Sens. 34, 7356–7368.
Yu, K., 2012. Coral reefs in the South China Sea: Their response to and records on past environmental changes. Sci. China Earth Sci. 55, 1217–1229.
Zhang, Q., Pandey, B., Seto, K.C., 2016. A Robust Method to Generate a Consistent Time Series From DMSP/OLS Nighttime Light Data. Ieee T Geosci. Remote 54, 5821–5831.
Zhao, M., Zhou, Y., Li, X., Zhou, C., Cheng, W., Li, M., Huang, k., 2019a. Building a Series of Consistent Night-Time Light Data (1992-2018) in Southeast Asia by Integrating DMSP-OLS and NPP-VIIRS. Ieee T Geosci. Remote 58, 1–14.
Zhao, X., Yu, B., Liu, Y., Chen, Z., Li, Q., Wang, C., Wu, J., 2019b. Estimation of Poverty Using Random Forest Regression with Multi-Source Data: A Case Study in Bangladesh. Remote Sens. 11, 375.
Zheng, Q., Weng, Q., Wang, K., 2019. Developing a new cross-sensor calibration model for DMSP-OLS and Suomi-NPP VIIRS night-light imageries. Isprs J. Photogramm. 153, 36–47.